Journal of
Laser Applications

RESEARCH ARTICLE | DECEMBER 14 2023

Influence of temperature and beam size on weld track shape in laser powder bed fusion of pure copper using near-infrared laser system

Special Collection: Proceedings of the International Congress of Applications of Lasers & Electro-Optics (ICALEO 2023)

Alexander Bauch ; Dirk Herzog

J. Laser Appl. 36, 012007 (2024)
https://doi.org/10.2351/7.0001118

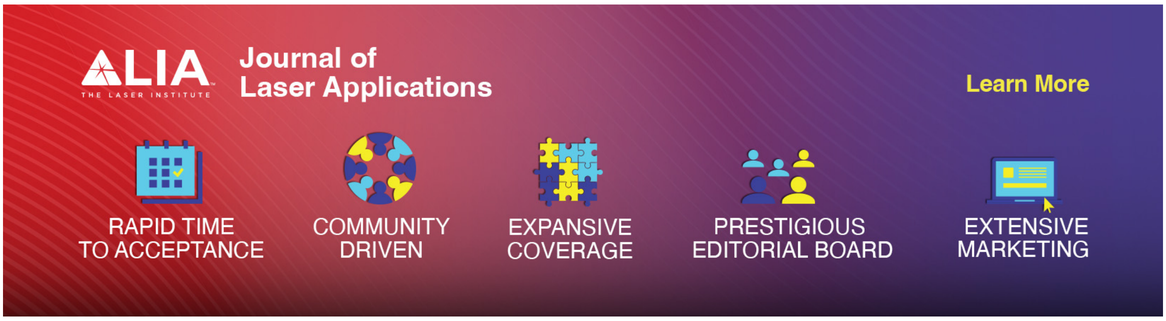

Journal of
Laser Applications

ARTICLE

pubs.aip.org/lia/jla

Influence of temperature and beam size on weld track shape in laser powder bed fusion of pure copper using near-infrared laser system

Cite as: J. Laser Appl. **36**, 012007 (2024); doi: 10.2351/7.0001118
Submitted: 26 June 2023 · Accepted: 22 November 2023 ·
Published Online: 14 December 2023

View Online Export Citation CrossMark

Alexander Bauch[1] and Dirk Herzog[2]

AFFILIATIONS

[1] Fraunhofer Research Institution for Additive Manufacturing Technologies IAPT, Am Schleusengraben 14, 21029 Hamburg, Germany
[2] Hamburg University of Technology, Institute for the Industrialization of Smart Materials, Am Schleusengraben 14, Hamburg 21029, Germany

Note: Paper published as part of the special topic on Proceedings of the International Congress of Applications of Lasers & Electro-Optics 2023.

ABSTRACT

Additive manufacturing of copper using laser powder bed fusion enables the production of highly complex components with excellent heat and electrical conductivity. However, the processing of copper by means of near-infrared laser radiation, which is commonly used, is challenging due to its high reflectivity. Nevertheless, it has been demonstrated that high densities and electrical conductivities can be achieved using high-power laser systems. In order to process pure copper with reliable quality with different machines, it is essential to understand the conditions at which a continuous weld track is formed. For this purpose, weld tracks with varying laser power and scan speeds were welded on a copper substrate plate with an applied powder layer. The preheating temperature of the substrate plate and the beam size were varied to test different process conditions. The melt pool depths and widths were measured, and a relationship was elaborated. Based on these results, cube samples with discrete weld tracks on top were manufactured. The melt pool depth was measured and compared with the predicted melt pool depth to investigate the transferability of the elaborated relationship from the substrate to process conditions. It was found that with rising preheating temperature and for larger beam diameters at the same peak intensity, the weld width and weld depths increase. Furthermore, continuous weld tracks formed reliably in the keyhole welding regime. A good agreement between the weld depth of weld tracks on the substrate and the elaborated relationship was revealed. However, the weld tracks were shallower than predicted.

Key words: pure copper, laser powder bed fusion, near-infrared laser system, scaling laws, additive manufacturing

INTRODUCTION

The high thermal and electrical conductivity of copper makes it an ideal material for heat sinks, heat exchangers, and induction coils. The high design freedom of additive manufacturing in combination with the excellent material properties offers new possibilities for optimized and, thus, more efficient components. In addition to binder jetting and electron beam powder bed fusion, laser powder bed fusion (LPBF) is a possible additive manufacturing technology for pure copper. However, high reflectivity for near-infrared (NIR) laser radiation makes pure copper challenging to process.[1] In this context, switching to a laser system emitting in the green spectrum offers a significant advantage.[2] However, such laser systems are currently used only in dedicated equipment, making NIR laser systems most widely used in LPBF machines due to their significant cost advantage and beam quality. For that reason, solutions such as coated copper powder[3–5] or preheating the build plate[6] have been investigated. However, impurities and oxidation at elevated temperatures have a negative impact on the electrical conductivity.[3–6]

Densities up to 99.8% and electrical conductivity of up to 94% compared to the international annealed copper standard (IACS) are reported for LPBF using NIR laser radiation of pure copper in

TABLE I. Physical properties of copper at the melting point taken from Ref. 11.

Property	Symbol (unit)	Value
Density	ρ (kg/m^3)	8295
Heat capacity	c_p (J/(kg K))	469
Thermal diffusivity	α (mm^2/s)	83
Latent heat of fusion	L_M (kJ/kg)	209
Melting temperature	T_M (K)	1357

the transition zone between conduction and keyhole welding.[7] However, weld track formation in LPBF has been investigated only for beam diameters smaller than 45 μm and laser powers up to 600 W.[1,7] Current LPBF machines are equipped with laser systems offering a laser power of up to 1000 W and wider beam diameters, so there is a need for further investigations.

During the LPBF process, heat accumulation can occur, which can cause distortions or pores.[8] To understand under which conditions continuous weld tracks reliably form can, therefore, enhance process stability as well as enable the transfer of process parameters from one machine to another. It was found by King *et al.* that experimental and simulation results for different materials and laser parameters converge to a single curve, when plotted against the normalized enthalpy.[9] The normalized enthalpy ($\Delta H/h_s$), given in Eq. (1), describes the ratio between the energy input and the enthalpy at melting and was derived by Hann *et al.* from dimensionless parameter groups.[10] The energy input includes the beam diameter σ, the scan speed u, and the thermal diffusivity α. The enthalpy can be calculated by using Eq. (2), and the physical properties of copper are given in Table I. The temperature difference ΔT is calculated between melting temperature T_M and ambient temperature T_0,

$$\frac{\Delta H}{h_s} = \frac{A\,P}{h_s\,\sqrt{\pi\,\alpha\,\sigma^3\,u}}, \tag{1}$$

$$h_s = \rho\left(c_p \Delta T + L_M\right). \tag{2}$$

The absorptivity A of copper powder in LPBF for NIR laser radiation in the heat conduction regime is around $A_C = 0.2$.[1] Due to keyhole formation, the absorptivity increases in the transition regime and saturates in the keyhole regime at $A_K = 0.53$.[1] The process regimes can be identified based on the aspect ratio of weld depth to weld width $R = d/w$. Keyhole formation is initiated when the melt pool front exceeds an inclination angle of 45°, which corresponds to $R = 0.5$.[12] Though this was found for the bulk material, a transfer to a stable LPBF process appears valid due to laser absorption occurring mainly inside the melt pool.[13] A fully developed keyhole is expected for $R > 0.8$, which indicates an elongated melt pool and deep substrate penetration.[14]

The normalized enthalpy is useful to scale process parameters between different machines, materials, and layer thicknesses to increase productivity.[9,10,15–17] However, the normalized enthalpy does not include additional physics in the keyhole regime.[9] Specifically, for materials with high heat conductivity, such as copper, suitability has to be examined.

In this study, the beam diameter and the preheating temperature of the build plate were varied to understand the influence of different process conditions on weld track formation of pure copper. For that reason, individual weld tracks were welded on the build plate with varying laser power and scan speed. A relationship for weld width and weld depth is formulated by means of normalized enthalpy. Additionally, individual weld tracks were printed on top of cubes to investigate the transferability of the relationship to process conditions in the steady state.

EXPERIMENT PROCEDURE AND METHODS

Laser process

Experiments were carried out using two different machine setups to vary the beam diameter without defocusing the laser beam. A beam diameter D4σ of 88 and 62 μm was calculated for machine setup 1 and machine setup 2, respectively. For the calculation, a gaussian distribution was fitted to the measurement data. Beam profile measurements were carried out at 150 W using a CCD camera SP928 equipped with an LBS-300 beam splitter (Ophir Spiricon Europe GmbH, Germany) that passes 0.01% of the input laser beam to the camera. Additionally, the laser beam was attenuated after the beam splitter by two neutral density filters, which results in a total of ND4.

Machine setup 1

AconityLab (Aconity 3D GmbH, Germany) equipped with a 1 kW fiber laser (Coherent Inc., USA) emitting at a wavelength of 1070 nm and a resistive heating platform for preheating temperatures of up to 500 °C.

Machine setup 2

DMP Flex 350 (3D Systems Inc., USA) equipped with a 1 kW fiber laser (IPG Laser GmbH, Germany) emitting at a wavelength of 1070 nm.

Material

Pure copper powder Cu OFHC (ECKART TLS GmbH, Germany) with a purity of >99.95% Cu and a spherical particle shape were used. The particle size distribution was 15.7, 31.8, and 45.5 μm for D10, D50, and D90, respectively. The measurement was carried out by dynamic image analysis using a Camsizer X2 (Microtrac Retsch GmbH, Germany). Cu-HCP was chosen as the substrate material.

Experimental design

Two experiments were conducted. First, individual weld tracks were welded onto the substrate to identify the influence of preheating temperature and beam size on the weld track geometry. Second, discrete weld tracks were printed directly on top of solid cubes to investigate differences to realistic process conditions. Both experiments were carried out under an inert atmosphere using argon. Preheating of the substrate, laser processing, and cooling down

TABLE II. Overview of used process parameters for weld tracks on the substrate.

Parameter		Limit Lower	Limit Upper	Step size
Laser power	(W)	400	1000[a]	100
Scan speed	(mm/s)	200	1000	100

[a] Laser power of machine setup 1 was limited to 900 W due to losses inside the beam path.

were conducted below a 100 ppm oxygen to limit oxidation of the copper powder. The respective preheating temperature was held for 1 h to ensure the heating of the top side and the powder layer. Additionally, the substrate was abrasively blasted to ensure a uniform surface finish.

Weld tracks on the substrate

To achieve a constant powder layer thickness across all experiments, a pocket with a depth of 90 μm was machined into the copper substrate using milling and filled with copper powder. A steel blade was used to remove excessive powder. Individual weld tracks were welded with varying laser power and scan speed. The limits and step size of the full factorial experimental plan are given in Table II.

The experimental plan was run with every preheating temperature and machine setup listed in Table III. It must be noted that the substrate plate for machine setup 1 was split into upper and lower halves, and the respective experimental run was conducted on one of the halves so that two preheating temperatures were used on one substrate plate, e.g., RT and 100 °C.

Weld tracks on cubes

Solid cubes with a size of $10 \times 10 \times 10\ \text{mm}^3$ and three discrete weld tracks on top were printed using machine setup 2, and the process parameters given in Table IV. The process parameters were selected based on the findings of the weld tracks on substrate experiments. A layer thickness of 45 μm and a rotation of 67° between layers were used. The weld tracks on top were printed with a 90° rotation relative to the previous layer and parallel to the outer edge.

Weld track classification

A digital microscope VHX-5000 (Keyence Deutschland GmbH, Germany) was used to take images of the weld tracks. Weld tracks were categorized into the following three categories based on their regularity.

TABLE III. Overview of the used machine setups.

Machine setup	D4σ (μm)	Preheating temperature (°C)
1.	88	Room temperature, 100, 200, 300, 400, and 500
2.	62	Room temperature

TABLE IV. Overview of process parameters for the solid cubes and the respective weld tracks on top.

Parameter field	Normalized enthalpy (–)	Hatch distance (μm)
1	8.54, 9.55, 10.25, 11.46, 11.95, 13.36	120, 130, 140, 150
2	12.47, 13.66, 14.03, 15.37	130, 140, 150, 160

1. Continuous: The weld track is regular and has no gaps.
2. Occasionally broken: The weld track has few narrow gaps.
3. Discontinuous: Formation of single segments and droplets with significant gaps in the weld track.

An example for each category is shown in Fig. 1.

Specimen preparation

Cross sections of the weld tracks on the substrate plate and on top of the cubes were prepared to measure the weld width w and weld depth d according to the scheme outlined in Fig. 2. The weld tracks were mechanically cut in the middle perpendicular to the scan direction, cold mounted, and metallographically prepared using a silicon carbide grinding paper. Final polishing was achieved with diamond suspension followed by OP-S. To reveal the microstructure, the specimens were etched in a hot ammonium persulfate solution (10%). Cross section images were taken using an inverted optical microscope GX-51 equipped with a camera UC30 (Olympus, Germany).

WELD TRACK ON THE SUBSTRATE

In the following, the influence of the beam size and preheating temperature is presented for a typical set of weld tracks on the substrate with a scan speed of $v = 500$ mm/s. The filling of the marker indicates the classification of the weld track according to the previous definition. The median difference between both evaluated sides of the weld track experiment was 15.84 μm for weld width and 13.05 μm for weld depth.

Influence of beam size

An increase in weld width and weld depth with increasing peak intensity I_0, which is related directly to the laser power, can be

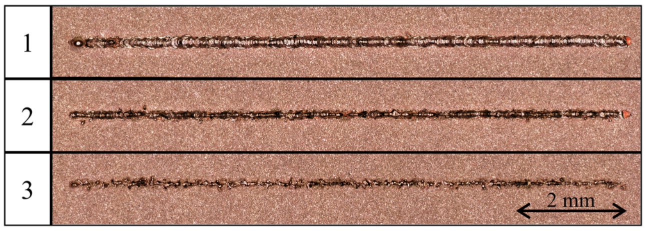

FIG. 1. Exemplary weld tracks for each category: 1. Continuous, 2. Occasionally broken, 3. Discontinuous.

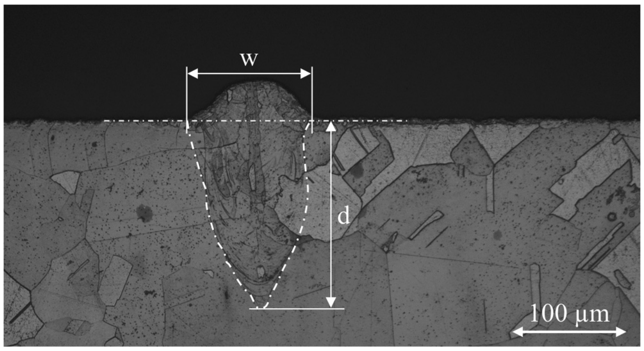

FIG. 2. Exemplary cross section of a weld track with weld width w and weld depth d.

observed in Fig. 3 for a typical data set. The aspect ratio was used to identify the transition from heat conduction welding ($R < 0.5$) to keyhole formation ($0.5 < R < 0.8$) and keyhole welding ($R > 0.8$). The transition points are critical for the welding process because the absorption coefficient changes. In conduction welding, the absorption coefficient is more or less constant, but during keyhole formation, the absorption coefficient rises and saturates when the keyhole is completely formed.[1,18,19]

Since the transition point cannot be identified exactly, a transition area is marked in gray. A linear fit is used to reveal the trend in the respective intervals below and above the transition region. The vertical line has been placed in the center of the transition area, and the fit was extended to this center line to highlight possible jumps in weld width and weld depth.

Cross sections above and below the transition area for a beam diameter of 88 μm are displayed in Fig. 4. With increasing peak intensity from (a) to (d), the shape of the melt pool changes from semicircular, which is characteristic for heat conduction welding ($R < 0.5$), to a U-shape with intermediate substrate penetration, which is characteristic for keyhole formation. Comparing the increase in weld width and weld depth from (a) to (b) with that from (b) to (c), a significant rise is noticeable. This indicates a significant jump in absorptivity due to the onset of multireflection. With further increase in peak intensity (d), the weld width and weld depth increase, but the aspect ratio indicates a stronger increase in weld depth. This trend is also apparent in Fig. 3.

For the beam diameter of $\sigma = 62\,\mu$m, the aspect ratio indicates that the keyhole formation ($0.5 < R < 0.8$) occurs entirely in the transition area. This is confirmed by the cross-section images in Fig. 5. With increasing peak intensity from (a) to (b), the shape of the melt pool changes from semicircular, which is characteristic for heat conduction welding ($R < 0.5$), to a deep penetrating U-shape due to multireflection inside the keyhole ($R > 0.8$). With increasing intensity from (b) to (d), the keyhole depth increases but the melt pool width around the keyhole perpendicular to the scan direction remains more or less constant, which is also apparent in Fig. 3. This indicates that the high thermal conductivity of pure copper inhibits the expansion of the melt pool perpendicular to the scan direction, and, thus, only a limited melt pool exists around the keyhole cavity. Therefore, the dimension of the melt pool depends on the width and depth of the keyhole cavity. Due to the multireflection and thus energy transfer to the tip of the keyhole, the cavity of the keyhole becomes deeper with increasing intensity. However, the Gaussian energy distribution causes the width of the cavity to increase only slightly with increasing intensity.

Comparing the beam diameters of 88 and 62 μm at a peak intensity of $I_0 = 26$ MW/cm^2 in Fig. 3, it is noticeable that heat conduction welding ($R < 0.5$) is present for a beam diameter of 62 μm, whereas keyhole formation ($R > 0.5$) is present for a beam diameter of 88 μm. As shown by Cunningham *et al.*,[20] the

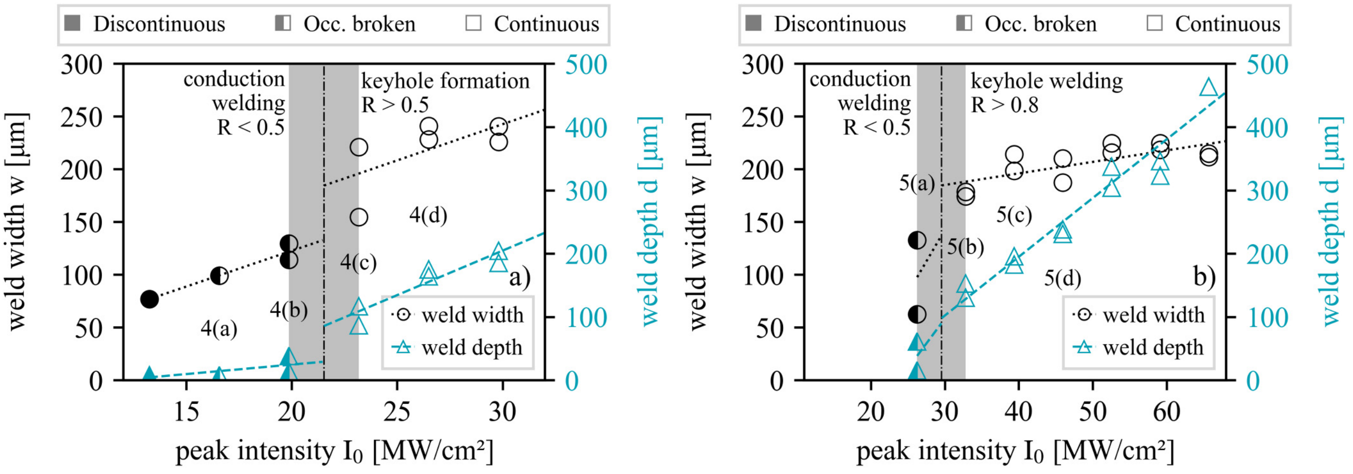

FIG. 3. Influence of peak intensity I_0 on weld width w and weld depth d for v = 500 mm/s and a laser beam diameter of left: $\sigma = 88\ \mu$m and right: $\sigma = 62\ \mu$m on the substrate. The numbers and letters refer to Figs. 4 and 5.

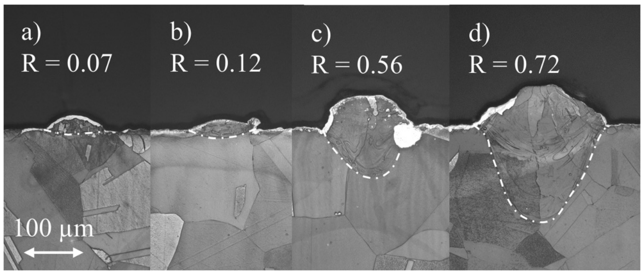

FIG. 4. Weld track cross section and aspect ratio for peak intensities I_0 of (a) 17, (b) 20, (c) 23, and (d) 26 MW/cm² for $\sigma = 88$ μm and v = 500 mm/s.

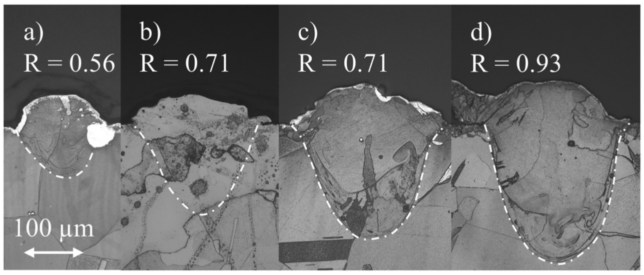

FIG. 6. Weld track cross section and aspect ratio at P = 700 W and a v = 500 mm/s for preheating temperature of (a) RT, (b) 200, (c) 400, and (d) 500 °C.

interaction time between the laser and material is a critical factor for keyhole formation. Increasing the interaction time while the laser power remains the same results in higher energy input into the material, causing more material to melt. In addition, the formation of a keyhole significantly increases the absorption,[1] which leads to a further increase in energy input and thus to an even larger amount of molten material. In laser powder bed fusion, the interaction time of the laser beam is the beam diameter divided by the scan speed $t_i = \sigma/v$. The interaction time increases for larger beam diameters at a constant scan speed, so that keyhole formation occurs at lower intensities. In addition, a larger beam diameter at the same peak intensity results in a wider weld width since the energy required for melting can be achieved over a wider region. Therefore, wider and deeper weld tracks are observed for larger beam diameters at the same intensity. However, it should be noted that the achievable peak intensity for larger beam diameters is limited by the used laser systems with typical laser powers for LPBF of up to 1 kW.

Considering Fig. 3, discontinuous or occasionally broken weld tracks only occur for conduction welding (R < 0.5). In the keyhole formation regime (R > 0.5), continuous weld tracks form.

Influence of preheating temperature

In Fig. 6, cross sections for different preheating temperatures at a laser power of P = 700 W and a scan speed of v = 500 mm/s are displayed. One can recognize that the weld width and weld depth increase with rising preheating temperature. Furthermore, the increase in the aspect ratio indicates that keyhole formation is promoted by rising preheating temperature.

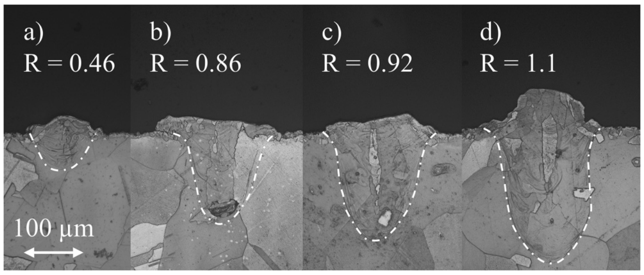

FIG. 5. Weld track cross section and aspect ratio for peak intensities of (a) 26, (b) 33, (c) 39, and (d) 46 MW/cm² for $\sigma = 62$ μm and v = 500 mm/s.

The aspect ratio was used to identify the transition from heat conduction welding (R < 0.5) to keyhole formation (R > 0.5). It was found that for room temperature and preheating temperatures of 100, 200, and 400 °C, the transition occurs between 600 and 700 W. For preheating temperatures of 300 °C, the transition took place between 500 and 600 W and for 500 °C, between 400 and 500 W. Despite some uncertainty due to the values measured at 400 °C, a trend to lower necessary laser power for keyhole initiation with increasing preheating temperature may still be assumed.

The corresponding weld width w and weld depth d are plotted in Fig. 7. A linear fit is used to reveal the trend in the respective intervals below (R < 0.5) and above (R > 0.5) the transition point. Since the transition point cannot be precisely determined, the trend line extends to the midpoint between the nearest points to highlight jumps in weld width and weld depth. In addition, the jump is marked with a vertical line. For a preheating temperature of 500 °C, a sharp drop in weld width and weld depth at a laser power of 800 W is present. Log files were checked, and the laser power was set correctly. Therefore, the authors assume that there was a local discontinuity in the powder layer or dust on the protective window. For this reason, the data point was excluded from the fitting.

The course of the trend lines confirms the findings that with increasing preheating temperature, the weld width and weld depth increase.

Considering the transition point from heat conduction welding (R < 0.5) to keyhole formation (R > 0.5), it can be recognized in Fig. 7 that continuous weld tracks formed at room temperature and preheating temperatures of 100 and 300 °C above the transition point. For a preheating temperature of 200 °C, an aspect ratio of R > 0.45 just below the transition point was already sufficient to form a continuous weld track. At preheating temperatures of 400 and 500 °C, continuous weld tracks were also formed below an aspect ratio of R < 0.5. This indicates the necessity of keyhole formation for continuous weld tracks at low preheating temperatures, as observed previously for the beam size without preheating. However, at high preheating temperatures, continuous weld tracks are even formed in the conduction welding regime. Such a positive influence of preheating on the weld track formation was also

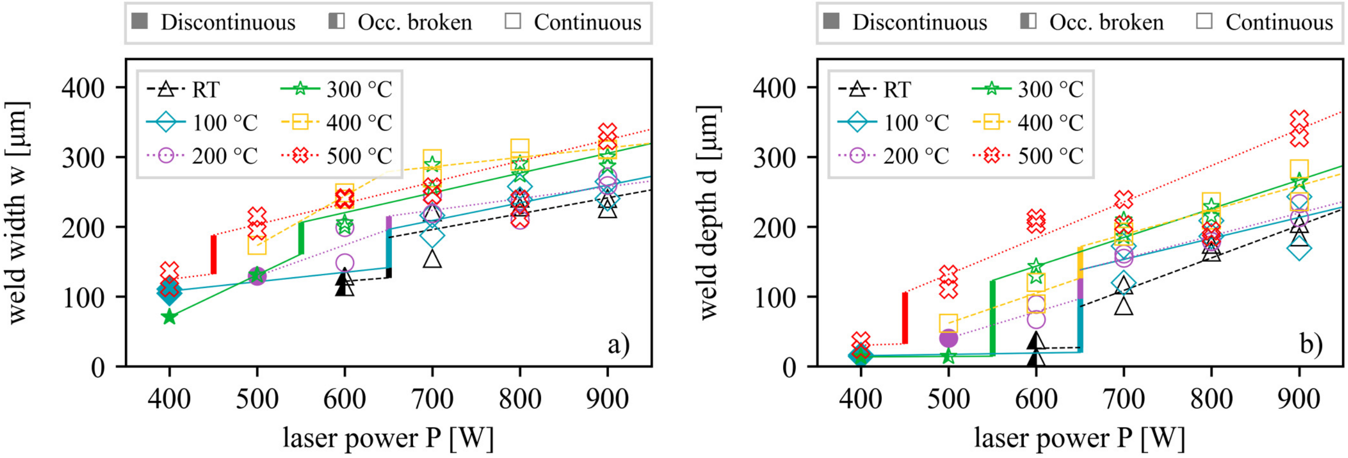

FIG. 7. Influence of preheating temperature on *left:* weld width w and *right:* weld depth d for $v = 500$ mm/s on the substrate. The trend line is split into two segments with $R < 0.5$ and $R > 0.5$.

shown by Malý *et al.*[6] In addition to the reduction in necessary energy for melting, a higher absorption due to oxidation, which could also be observed in this study by a color change of the remaining copper powder, better wetting conditions, and prolongation of the solidification times were mentioned as a reason. However, better wettability and prolonged solidification time could be valid explanations for continuous weld tracks without keyhole formation since the other phenomena would instead promote keyhole formation.

Overall, it can be recognized that an increase in preheating temperature leads to an enlarged melt pool, which can be expected from the additional heat input. Furthermore, continuous weld tracks form in a broader process parameter range. However, oxidation is a concern for the reusability of the powder.[6]

Process map for continuous weld tracks

In order to understand at which conditions continuous weld tracks are formed, the proportion in percent of discontinuous, occasionally broken, and continuous weld tracks as well as the corresponding cumulative distribution with regard to the aspect ratio R of all analyzed weld tracks are shown in Fig. 8. At low aspect ratios of $R = 0.1$, around 8% of weld tracks are continuous. The proportion of continuous weld tracks increases to 30% for an aspect ratio of $R = 0.5$, while the proportion of discontinuous tracks decreases significantly. The aspect ratio range of $R < 0.5$ covers 43.1% of all analyzed weld tracks, but continuous weld tracks are only formed with preheating temperatures of 400 and 500 °C. At an aspect ratio of $R = 0.8$, no discontinuous tracks are observed and only a small proportion of around 12% are categorized as occasionally broken. For higher aspect ratios, only continuous weld tracks are formed. At very high aspect ratios of $R > 2$, the proportion of occasionally broken weld tracks increases rapidly, but just 2.34% of all analyzed weld tracks have this aspect ratio.

Since continuous weld tracks begin to form at an aspect ratio of $R = 0.5$, the formation of a keyhole is necessary to achieve continuous weld tracks. Furthermore, discontinuous weld tracks are not present above an aspect ratio of $R > 0.8$, at which point, the transition from heat conduction welding toward keyhole welding is completed. Within the investigated parameter range, the condition for reliably achieving continuous weld tracks is consequently a

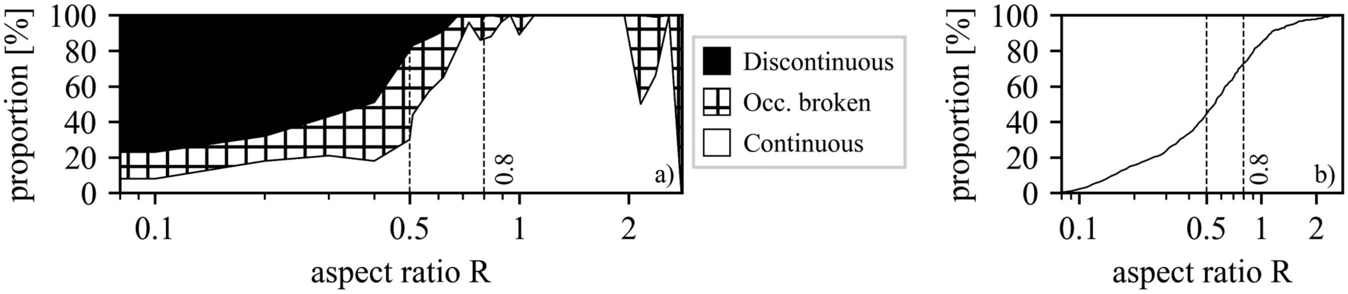

FIG. 8. Influence of aspect ratio R on (a) weld track categorization and (b) cumulative distribution.

completely formed keyhole. The only exception occurs at high preheating temperatures, for which heat conduction welding appears to be enabled either due to increased wettability or prolonged solidification time or due to a combination of both. At very high scan speeds $v \geq 900$ mm/s, occasionally broken weld tracks occur for aspect ratios of $0.8 < R < 1.1$ due to necking and humping. In addition, at very high aspect ratios ($R > 2$), a deep and narrow keyhole is formed, which tends to collapse and cause a short break in the weld track.

SCALING LAW FOR MELT POOL PREDICTION

In the previous section, it was described that the melt pool geometry depends on the intensity, which is related to the laser power and beam size, the interaction time, given by the beam diameter divided by the scan speed, and the preheating temperature. By using the normalized enthalpy, given in Eq. (1), all analyzed weld tracks can be combined in a single figure. Continuous weld tracks form reliably only for aspect ratios of $R \geq 0.8$. For this reason, only these weld tracks are considered, and a constant laser absorptivity $A_K = 0.53$ in the keyhole regime is assumed.[1]

The measured weld width and weld depth of all analyzed weld tracks in the keyhole welding regime are plotted in Fig. 9. The beam diameter σ is used as a characteristic length for normalizing the weld width and weld depth, since the size of the keyhole cavity, and thus, the melt pool depends on the beam diameter. A linear regression was chosen because a constant increase in weld depth and weld width is expected with rising energy input. Additionally, the 95% confidence interval (CI) is marked. The regression equation, the coefficient of determination R^2, and the root mean square error RMSE of the regression are given in Table V.

The normalized weld width and normalized weld depth increase with increasing normalized enthalpy. While there is good agreement between the regression and the measured data for the normalized weld depth, the normalized weld width reveals a significant discrepancy.

TABLE V. Results of linear fitting for normalized weld width and normalized weld depth.

Regression	R^2	RMSE
$w/\sigma = 0.16^*(\Delta H/hs) + .61$	0.52	0.48
$d/\sigma = 0.62^*(\Delta H/hs) - 3.43$	0.86	0.77

The authors assume that the high melt pool velocities during keyhole welding lead to major variations in weld width. Additionally, irregularities in the powder layer may contribute to the variations. Therefore, additional physics may need to be considered to estimate the width of the melt pool perpendicular to the scan direction during keyhole welding. The weld depth, on the other hand, depends mainly on the depth of the keyhole cavity and thus increases with rising energy input due to intensified multireflection.

The results indicate the possibility to scale process parameters among different machine setups and local thermal conditions based on the normalized enthalpy. Although it is a rather simple regression, it can be utilized to accelerate the parameter development for other equipment or to improve the process stability in terms of heat accumulation during the process in combination with preliminary simulations.

Difference between weld tracks on the substrate and on top of cubes

Since the process conditions in the actual printing process are not necessarily identical to those on the substrate plate due to the

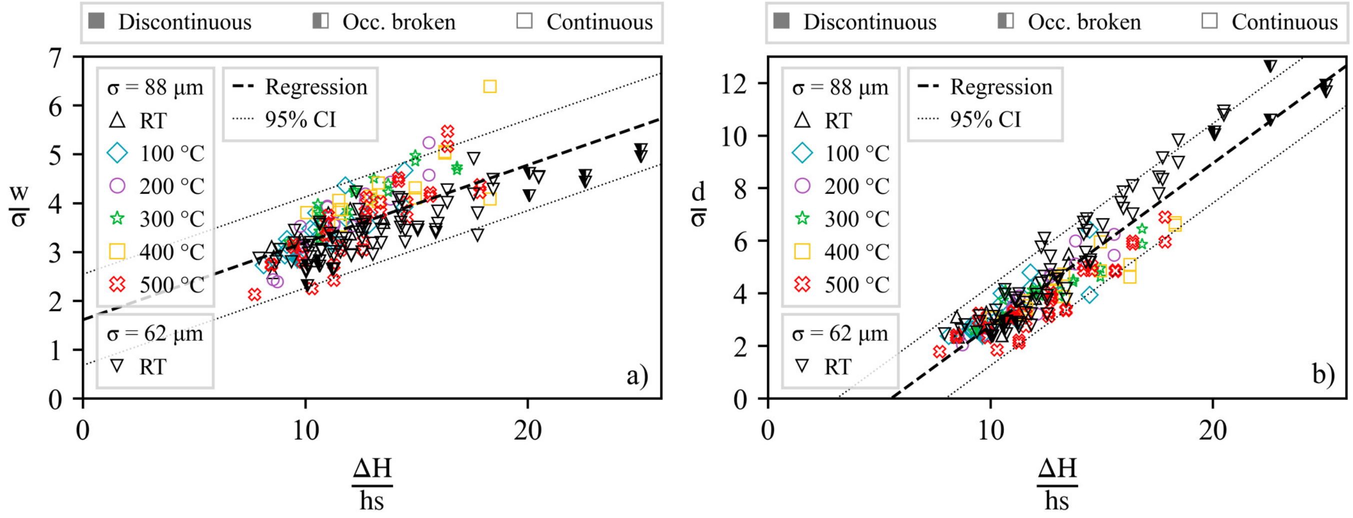

FIG. 9. Relationship between the normalized enthalpy and *left:* the normalized weld width and *right*: the normalized weld depth for different beam diameters σ and preheating temperatures.

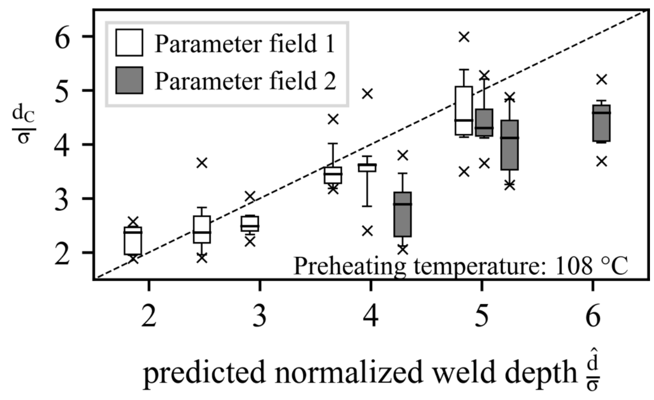

FIG. 10. Comparison of the normalized weld depth prediction $\hat{d}/\sigma$ and measured normalized weld depth d_C/σ on top of cubes.

transient behavior of the powder layer, the heat-up of the process zone, and further influences,[21,22] individual tracks were printed on top of cubes in order to investigate the transferability of the prediction. Only the normalized weld depth is examined, since only in this case a good agreement of the prediction is given. A temperature of 108 °C is considered for the prediction, although no preheating was used, since this temperature was measured by a thermocouple below the build plate at the time of exposure. However, the real temperature is expected to be above this value.

In Fig. 10, the normalized weld depth on top of the cubes d_C/σ is plotted against the predicted weld depth $\hat{d}/\sigma$. Data sets of cubes printed with different hatch distances but the same laser power and scan speed were combined to obtain a larger sample size. Each cube achieved a density between 97.3% and 99.3%, measured by region of interest over the entire cross-sectional area. For that reason, the influence of the hatch distance on the weld track geometry on top of the cubes was considered to be small and the data sets can therefore be combined.

On average, a difference between the normalized weld depth on top of the cubes and the predicted weld depth of −0.59 is found and thus the weld tracks are shallower than predicted. At the lowest normalized enthalpy, and thus the lowest predicted normalized weld depth, a positive deviation is noticed. The highest deviation between the predicted and the measured normalized weld depth occurs in parameter field 2 at predicted normalized weld depths of 5.02, 5.25, and 6.07. For parameter field 1, the average difference is significantly smaller, with a value of just −0.13.

Overall, good agreement between the predicted and the measured weld depths can be recognized for parameter field 1. However, one can notice that the normalized weld depth of weld tracks on top of cubes is lower than the predicted normalized weld depth. One reason for this could be the layer thickness. Yang *et al.* found that the weld depth decreases with increasing layer thickness.[23] The authors assumed a doubling of the layer thickness between the layer thickness in the steady state and the nominal layer thickness of the build process for the development of the prediction. The realistic value can therefore be even higher. In particular, considering that the local temperature is higher than the measured temperature below the build plate and thus an even higher weld depth would be predicted, this indicates an even higher layer thickness. Conversely, a high local (preheating) temperature can enhance powder oxidation and thus increase the absorptivity[4] and increase therefore the weld depth, while the layer thickness has no influence on absorptivity.[18] Further causes for differences can be the surface roughness and the associated quality and packing density of the powder layer.

CONCLUSIONS

In this work, the influence of preheating temperature and beam size on the weld width and weld depth during laser powder bed fusion of copper was investigated. It was found that lager beam diameters result in wider and deeper weld tracks at the same peak intensity due to a longer interaction time, which promotes keyhole formation, and sufficient energy to melt over a wider area. In addition, an increase in preheating temperature also promotes keyhole formation and reduces the remaining energy required for melting so that the weld width and weld depths rise. By categorizing the weld tracks into discontinuous, occasionally broken, and continuous weld tracks, it was found that continuous weld tracks form reliably under the condition of a completely developed keyhole at an aspect ratio of $R \geq 0.8$. Only at high preheating temperatures, continuous weld tracks form even in the conduction welding regime. A relationship for the normalized weld width and depth using the beam size as the characteristic length based on the normalized enthalpy was determined. Good agreement is found for the weld depth. However, weld tracks under actual process conditions, printed on top of cubes, are shallower than predicted by the relationship. The authors assume that the actual powder layer height may differ from the assumed layer height for the development of the relationship. Therefore, the powder layer thickness is another crucial factor that should be taken into account, as approached by Vaglio *et al.*[24] In addition to the developed relationship, other approaches such as machine learning are also conceivable to improve the quality of the prediction.

Nevertheless, the developed relationship demonstrates a basic suitability so that it can be used to transfer process parameters from one machine to another. Furthermore, in combination with a previous simulation of the thermal behavior, a process control by the developed relationship is conceivable.

ACKNOWLEDGMENTS

The work described in this paper is financed with funds from the state innovation funding of the Free and Hanseatic City of Hamburg by the Science, Research, Equality and Districts Authority (BWFGB) under the reference number LIF-004. The authors would like to thank Malte Schubert for tirelessly preparing and evaluating the micrographs.

AUTHOR DECLARATIONS

Conflict of Interest

The authors have no conflicts to disclose.

Author Contributions

Alexander Bauch: Conceptualization (lead); Data curation (lead); Formal analysis (lead); Funding acquisition (lead); Investigation (lead); Methodology (lead); Project administration (lead); Supervision (lead); Visualization (lead); Writing – original draft (lead); Writing – review & editing (supporting). **Dirk Herzog:** Conceptualization (supporting); Methodology (supporting); Visualization (supporting); Writing – review & editing (lead).

DATA AVAILABILITY

The data that support the findings of this study are available from the corresponding author upon reasonable request.

REFERENCES

[1] L. Gargalis, J. Ye, M. Strantza, A. Rubenchik, J. W. Murray, A. T. Clare, I. A. Ashcroft, R. Hague, and M. J. Matthews, "Determining processing behaviour of pure Cu in laser powder bed fusion using direct micro-calorimetry," J. Mater. Process. Technol. **294**, 117130 (2021).

[2] G. Nordet, C. Gorny, Y. Mayi, J. Daligault, M. Dal, A. Effernelli, E. Blanchet, F. Coste, and P. Peyre, "Absorptivity measurements during laser powder bed fusion of pure copper with a 1 kW cw green laser," Opt. Laser Technol. **147**, 107612 (2022).

[3] S. D. Jadhav, S. Dadbakhsh, J. Vleugels, J. Hofkens, P. van Puyvelde, S. Yang, J.-P. Kruth, J. van Humbeeck, and K. Vanmeensel, "Influence of carbon nanoparticle addition (and impurities) on selective laser melting of pure copper," Materials **12**(15), 2469 (2019).

[4] S. D. Jadhav, J. Vleugels, J.-P. Kruth, J. Van Humbeeck, and K. Vanmeensel, "Mechanical and electrical properties of selective laser-melted parts produced from surface-oxidized copper powder," Mater. Des. Process. Commun. **2**, 1 (2020).

[5] V. Lindström, O. Liashenko, K. Zweiacker, S. Derevianko, V. Morozovych, Y. Lyashenko, and C. Leinenbach, "Laser powder bed fusion of metal coated copper powders," Materials **13**(16), 3493 (2020).

[6] M. Malý, D. Koutný, L. Pantělejev, L. Pambaguian, and D. Paloušek, "Effect of high-temperature preheating on pure copper thick-walled samples processed by laser powder bed fusion," J. Manuf. Process. **73**, 924–938 (2022).

[7] S. D. Jadhav, L. R. Goossens, Y. Kinds, B. V. Hooreweder, and K. Vanmeensel, " Laser-based powder bed fusion additive manufacturing of pure copper," Addit. Manuf. **42**, 101990 (2021).

[8] G. Li, R. Ganeriwala, D. Herzog, K. Bartsch, and W. King, "Numerical and experimental investigation of the geometry dependent layer-wise evolution of temperature during laser powder bed fusion of Ti–6Al–4 V," Prog. Addit. Manuf. **8**, 961–975 (2022).

[9] W. E. King, H. D. Barth, V. M. Castillo, G. F. Gallegos, J. W. Gibbs, D. E. Hahn, C. Kamath, and A. M. Rubenchik, "Observation of keyhole-mode laser melting in laser powder-bed fusion additive manufacturing," J. Mater. Process. Technol. **214**, 2915 (2014).

[10] D. B. Hann, J. Iammi, and J. Folkes, "Keyholing or conduction—Prediction of laser penetration depth," in *Proceedings of the 36th International MATADOR Conference, Manchster, UK, 14–16 July 2021* (Springer, London, 2010), p. 275.

[11] K. C. Mills, *Recommended Values of Thermophysical Properties for Selected Commercial Alloys* (Woodhead, Materials Park, 2002).

[12] R. Fabbro, M. Dal, P. Peyre, F. Coste, M. Schneider, and V. Gunenthiram, "Analysis and possible estimation of keyhole depths evolution, using laser operating parameters and material properties," J. Laser Appl. **30**, 32410 (2018).

[13] S. A. Khairallah, A. T. Anderson, A. Rubenchik, and W. E. King, "Laser powder-bed fusion additive manufacturing: Physics of complex melt flow and formation mechanisms of pores, spatter, and denudation zones," Acta Mater. **108**, 36–45 (2016).

[14] T. T. Roehling, S. S. Wu, S. A. Khairallah, J. D. Roehling, S. S. Soezeri, M. F. Crumb, and M. J. Matthews, "Modulating laser intensity profile ellipticity for microstructural control during metal additive manufacturing," Acta Mater. **128**, 197–206 (2017).

[15] A. M. Rubenchik, W. E. King, and S. S. Wu, "Scaling laws for the additive manufacturing," J. Mater. Process. Technol. **257**, 234–243 (2018).

[16] J. S. J. Ten, F. L. Ng, H. L. Seet, and M. L. S. Nai, "Method to maximize the productivity of laser powder bed fusion systems through dimensionless parameters," J. Laser Appl. **34**, 12016 (2022).

[17] D. B. Hann, J. Iammi, and J. Folkes, "A simple methodology for predicting laser-weld properties from material and laser parameters," J. Phys. D: Appl. Phys. **44**, 445401 (2011).

[18] J. Ye, S. A. Khairallah, A. M. Rubenchik, M. F. Crumb, G. Guss, J. Belak, and M. J. Matthews, "Energy coupling mechanisms and scaling behavior associated with laser powder Bed fusion additive manufacturing," Adv. Eng. Mater. **21**, 1900185 (2019).

[19] K. Behler, D. Heussen, M. Kupper, N. Pirch, T. Lantzsch, and J. H. Schleifenbaum, "Energy coupling in laser powder bed fusion of copper using different laser wavelengths," in *Proceedings of the Lasers in Manufacturing Conference 2021* (WLT, 2021).

[20] R. Cunningham, C. Zhao, N. Parab, C. Kantzos, J. Pauza, K. Fezzaa, T. Sun, and A. D. Rollett, "Keyhole threshold and morphology in laser melting revealed by ultrahigh-speed x-ray imaging," Science **363**, 849–852 (2019).

[21] G. Mohr, K. Sommer, T. Knobloch, S. J. Altenburg, S. Recknagel, D. Bettge, and K. Hilgenberg, "Process induced preheating in laser powder Bed fusion monitored by thermography and its influence on the microstructure of 316L stainless steel parts," Metals **11**, 1063 (2021).

[22] C. Hagenlocher, P. O'Toole, W. Xu, M. Brandt, M. Easton, and A. Molotnikov, "Analytical modelling of heat accumulation in laser based additive manufacturing processes of metals," Addit. Manuf. **60**, 103263 (2022).

[23] J. Yang, J. Han, H. Yu, J. Yin, M. Gao, Z. Wang, and X. Zeng, "Role of molten pool mode on formability, microstructure and mechanical properties of selective laser melted Ti-6Al-4 V alloy," Mater. Des. **110**, 558–570 (2016).

[24] E. Vaglio, G. Totis, A. Lanzutti, Lf Fedrizzi, and M. Sortino, "A novel thermo-geometrical model for accurate keyhole porosity prediction in laser powder-Bed fusion," Prog. Addit. Manuf. (published online 2023).